# Probing modifications of General Relativity using current cosmological observations

Gong-Bo Zhao,[1] Tommaso Giannantonio,[2] Levon Pogosian,[3] Alessandra Silvestri,[4]
David J. Bacon,[1] Kazuya Koyama,[1] Robert C. Nichol,[1] and Yong-Seon Song[1]

[1] *Institute of Cosmology and Gravitation, University of Portsmouth, Dennis Sciama Building, Burnaby Road, Portsmouth, PO1 3FX, UK*
[2] *Argelander-Institut für Astronomie der Universität Bonn, Auf dem Hügel 71, D-53121 Bonn, Germany*
[3] *Department of Physics, Simon Fraser University, Burnaby, BC, V5A 1S6, Canada*
[4] *Kavli Institute for Astrophysics and Space Research, MIT, Cambridge, MA 02139, USA*

(Dated: May 13, 2010)

We test General Relativity (GR) using current cosmological data: the cosmic microwave background (CMB) from WMAP5 (Komatsu *et al.* 2009), the integrated Sachs-Wolfe (ISW) effect from the cross-correlation of the CMB with six galaxy catalogs (Giannantonio *et al.* 2008), a compilation of supernovae Type Ia (SNe) including the latest SDSS SNe (Kessler *et al.* 2009), and part of the weak lensing (WL) data from CFHTLS (Fu *et al.* 2008, Kilbinger *et al.* 2009) that probe linear and mildly non-linear scales. We first test a model where the effective Newton's constant, $\mu$, and the ratio of the two gravitational potentials, $\eta$, transit from the GR value to another constant at late times; in this case, we find that GR is fully consistent with the combined data. The strongest constraint comes from the ISW effect which would arise from this gravitational transition; the observed ISW signal imposes a tight constraint on a combination of $\mu$ and $\eta$ that characterizes the lensing potential. Next, we consider four pixels in time and space for each function $\mu$ and $\eta$, and perform a Principal Component Analysis (PCA) finding that seven of the resulting eight eigenmodes are consistent with GR within the errors. Only one eigenmode shows a $2\sigma$ deviation from the GR prediction, which is likely to be due to a systematic effect. However, the detection of such a deviation demonstrates the power of our time- and scale-dependent PCA methodology when combining observations of structure formation and expansion history to test GR.



## I. INTRODUCTION

As cosmological observations improve, new possibilities arise for testing the physics that governs the evolution of our Universe. Precise all-sky measurements of the CMB by the WMAP satellite [1] have established that cosmic structure developed from a nearly scale-invariant initial spectrum of adiabatic fluctuations [2]. Baryon acoustic oscillations from SDSS [3] and growing catalogs of supernovae [4], in combination with the CMB, have tightened the constraints on the background expansion history, indicating a strong preference for the cosmological concordance model, ΛCDM. Correlating the CMB anisotropies from WMAP with wide-sky catalogs of galaxy counts have made it possible to detect the ISW effect [5, 6], obtaining independent evidence for the accelerating expansion of the Universe [7, 8]. Weak Lensing measurements by surveys such as COSMOS [9, 10] and CFHTLS [11, 12] have afforded the use of shear correlation functions and power spectra in order to test cosmology.

In parallel, the problem of cosmic acceleration has motivated explorations of new theoretical ideas, including the possibility that GR may be modified on large scales. Anticipating the substantial improvement in cosmological data sets that is expected with surveys such as DES [13], Pan-STARRS [14], LSST [15] and Euclid [16], model-independent frameworks for testing GR against observations of the growth of cosmic structures have been developed [17–26]. Recently, there has been progress towards a consensus on what properties such a framework should have [21, 25, 26]. First, it should be general, i.e. it should be able to describe a wide range of modified gravity models. Second, it should not violate the consistency of super-horizon sized perturbations with the background expansion. Third, it should involve as few parameters as possible, while still being flexible enough to capture most of the significant information contained in the data.

A good pragmatic starting point is to look for evidence of departures in the fundamental relationships among the perturbative fields familiar in cosmology: matter density and velocity perturbations, and the metric perturbations [19, 27–29]. It is commonly agreed that one needs two general functions of scale and time, in addition to the conservation of energy-momentum, to specify the evolution of the linear perturbations. For example, one can introduce $\mu$, relating the gravitational potential to the density contrast, and $\eta$, which relates the gravitational potential to the spatial curvature. Given these functions, it is possible to calculate the cosmological perturbations and all the observables with a full Boltzmann integration code, such as `MGCAMB` [25, 26].

The actual parametrization of the functions has not yet been researched as fully. The goal is to strike a balance between simplicity, i.e. working with as few parameters as possible, and allowing for enough flexibility in these functions to capture all of the information contained in the data. For example, one can discretize $\mu(k,z)$ and $\eta(k,z)$ on a grid in $(k,z)$ space and treat their values at each grid point, which we will call *pixels*, as independent parameters [30]. Motivated by simplicity, one might wish to start with the simplest possible model, such as con-

stant values of $\mu$ and $\eta$, and add complexity only if the fitted parameter values of this simple model show hints of departure from ΛCDM. However, this logic may not work in modified gravity studies and might lead to missing important information contained in the data. As the PCA analysis in [30] shows, the shapes of the well constrained eigenmodes suggest a higher sensitivity to scale-dependent features in $\mu$ and $\eta$, compared to their average values or the time dependence.

In this work, we first use a Fisher forecast-based PCA to determine the minimum number of pixels necessary to describe the shape of the best constrained eigenmodes of $\mu$ and $\eta$. We then use a Monte Carlo Markov Chain (MCMC) algorithm to fit these parameters to a combination of the available data, including CMB, ISW, SNe and WL, and find constraints on their de-correlated combinations. Throughout the paper we assume that the background expansion is given by the flat ΛCDM model which is strongly favored by the current constraints on the expansion history, and look for deviations from its predictions for the density perturbations. From a theoretical perspective, flatness is motivated by the inflationary origin of the Universe, and the viable models of modified gravity studied in the literature tend to be indistinguishable from ΛCDM at the background level.

Other tests of GR have been performed, in which different choices were made for the functions $\mu$ and $\eta$ (or a related set of parameters). In [31, 32] they were taken to have a specific form of time dependence, while in [33] they have a specific form of time and scale dependence; finally, [32] allowed them to vary in three redshift bins. The results of these studies show a good consistency with ΛCDM. To compare with the results of some of these studies, we consider a single-transition-in-redshift model in addition to our scale-dependent PCA method, generally finding a good agreement with GR. In addition to allowing for scale-dependence, other important differences between our study and the treatment in [32] include using the ISW cross-correlation data, using the CFHTLS WL data coming only from linear and mildly non-linear scales, and simultaneously varying two functions $\mu$ and $\eta$, while [32] varied them one at a time when working with a 3-bin model. The key conceptual difference from [33] is that we do not use WL data from a deeply non-linear regime, and we do not assume a specific scale and time dependence of the functions $\mu$ and $\eta$, but rather perform a PCA of their values on a gird in $(k, z)$.

We find that the agreement with ΛCDM is statistically more significant when no scale-dependence is allowed. After performing a PCA, we find that seven of the eight eigenmodes are consistent with GR within the errors. One eigenmode shows a $2\sigma$ deviation from the GR prediction, but can be directly traced to a feature in the WL aperture mass dispersion spectrum at 120 arc min, which is most likely caused by a systematic [34]. However, the detection of this effect shows the benefits of adopting a more flexible scale-dependent pixellation of $\mu$ and $\eta$, and demonstrates that using scale-independent methods could potentially hinder the detection of new physics, or, as in this case, simply the better understanding of the data.

The paper is organized as follows. Section II reviews the data sets used in this work. After describing our parametrization in Section III, we present the constraints on departures from GR in Section IV, and finally draw conclusions in Section V.

## II. OBSERVABLES AND DATA

In this section, we summarize the observables that will be used to constrain deviations from GR, and explain the data sets for these observables.

### A. Integrated Sachs-Wolfe effect

The ISW effect [5] is a secondary anisotropy of the CMB which is created whenever the gravitational potentials are evolving in time. This is due to the net energy gain that the CMB photons acquire when traveling through varying potential wells, and it is therefore a direct probe of the derivatives of the potentials $\Phi, \Psi$. In more detail, this effect generates additional CMB temperature anisotropies in any direction $\hat{\mathbf{n}}$ given by

$$\Theta_{\rm ISW}(\hat{\mathbf{n}}) \equiv \frac{\Delta T_{\rm ISW}}{T_{\rm ISW}}(\hat{\mathbf{n}}) = -\int \left(\dot{\Phi} + \dot{\Psi}\right)[\tau, \hat{\mathbf{n}}(\tau_0 - \tau)]\, d\tau, \tag{1}$$

where $\tau$ is the conformal time, the dot represents a conformal time derivative and the integral is calculated along the line of sight of the photon.

A direct measurement of this effect is difficult, due to the overlap with the primary CMB anisotropies, whose amplitude is at least 10 times bigger. An additional problem is that the ISW signal is biggest on the largest angular scales, which are most affected by cosmic variance. It is nevertheless possible to detect this signal by cross-correlating the full CMB with some tracers of the large-scale structure (LSS) of the Universe [6]: the primary CMB signal, generated at early times, is expected to have null correlation with the LSS, while the ISW anisotropies, produced at low redshift, correlate with the LSS distributions since they trace the fluctuations in the potentials.

We can then use a galaxy survey with visibility function $dN/dz(z)$ as a tracer of the LSS, and we can write the galaxy density fluctuation in a direction $\hat{\mathbf{n}}_1$ as

$$\delta_g(\hat{\mathbf{n}}_1) = \int b_g(z) \frac{dN}{dz}(z)\, \delta_m(\hat{\mathbf{n}}_1, z)\, dz, \tag{2}$$

where $b_g$ is the galaxy bias and $\delta_m$ the matter density perturbation. On the other hand, the ISW temperature anisotropy in a direction $\hat{\mathbf{n}}_2$ is given by

$$\Theta_{\rm ISW}(\hat{\mathbf{n}}_2) = -\int e^{-\kappa(z)} \frac{d}{dz}\left(\Phi + \Psi\right)(\hat{\mathbf{n}}_2, z) dz, \tag{3}$$

where $e^{-\kappa(z)}$ is the photons' visibility function and $\kappa$ the optical depth. After choosing a particular data set for the CMB and the LSS, we can then define the auto- and cross-correlation functions as

$$c^{Tg}(\vartheta) \equiv \langle \Theta(\hat{\mathbf{n}}_1)\, \delta_g(\hat{\mathbf{n}}_2)\rangle \quad (4)$$
$$c^{gg}(\vartheta) \equiv \langle \delta_g(\hat{\mathbf{n}}_1)\, \delta_g(\hat{\mathbf{n}}_2)\rangle, \quad (5)$$

where $\Theta$ is the full CMB temperature anisotropy and the averages are calculated over all pairs at an angular separation $\vartheta = |\hat{\mathbf{n}}_1 - \hat{\mathbf{n}}_2|$. Alternatively, the above calculation can be written in harmonic space, and the auto- and cross-power spectra are then derived.

We use the ISW data from [7], which were obtained by cross-correlating multiple galaxy catalogs with the CMB maps from WMAP. The data used trace the distribution of the LSS in various bands of the electromagnetic spectrum, with median redshifts $0.1 < \bar{z} < 1.5$, and consist of six catalogs (infrared 2MASS, visible SDSS main galaxies, luminous red galaxies and quasars, radio NVSS, and X-ray HEAO). This is an approximation of a true tomographic study of the ISW signal.

All maps were pixellated on the sphere, with a pixel size of 0.9 deg. The measurements were done in real space, calculating the angular cross-correlation functions (CCFs) between the maps. These were linearly binned in steps of 1 deg for angles 0 deg $\leq \vartheta \leq$ 12 deg; so the data set consists of 78 points $(c_i^{Tg})_{\rm obs}$.

A well known property of the correlation functions is that their data points are highly correlated; in this case, in particular, the high degree of correlation is present also between data points belonging to different catalogs, due to the partial overlaps in redshift and in sky coverage of the sources. For this reason, the full covariance matrix between all data points $\mathbf{C}_{ij}$ is a very important piece of information, and it was estimated in [7] using several Monte Carlo and jack-knife methods. Here we use the matrix produced with the most complete technique, a full Monte Carlo method where both galaxies and CMB maps were simulated and then correlated to measure the expected noise and covariance.

The calculation of the likelihood of a particular model given the ISW data is done as follows. First, the theoretical CCFs $(c_i^{Tg})_{\rm theo}$ and auto-correlation functions (ACFs) are calculated with a full Boltzmann integration within `MGCAMB`, based on the redshift distributions of the sources. The galaxy bias parameters are assumed to be independent and constant for each catalog, and are rescaled for each model imposing that the ACFs on small angular scales match the observations. Finally, the theoretical CCFs are multiplied by this rescaled bias to calculate the $\chi^2_{\rm ISW}$ distribution, given by

$$\chi^2_{\rm ISW} = \sum_{ij} \left[(c_i^{Tg})_{\rm obs} - (c_i^{Tg})_{\rm theo}\right] \left[\mathbf{C}^{-1}\right]_{ij} \times \left[(c_j^{Tg})_{\rm obs} - (c_j^{Tg})_{\rm theo}\right]. \quad (6)$$

### B. Supernovae and Cosmic Microwave Background

For the SNe data, we use the sample combination labeled ($e$) shown in table 4 of [4], which is a compilation of the SDSS-II SNe sample plus Nearby SNe, ESSENCE, SNLS and HST. To calculate the SNe likelihood, we use values from the `MLCS2K2` light curve fitter, and marginalize over the nuisance parameter, which is the calibration uncertainty in measuring the supernova intrinsic magnitude. Note that [4] found a discrepancy of the constraints on the F$w$CDM model (standard CDM model in a flat Universe plus a dark energy component with a constant $w$) using the two SNe fitters `MLCS2K2` and `SALT-II`. However, the discrepancy is much smaller (within $1\sigma$) for a flat $\Lambda$CDM model as shown in Tables 13 and 17 in [4], namely,

$$\Omega_{\rm m} = 0.312 \pm 0.022({\rm stat}) \pm 0.001({\rm syst}) \quad (\texttt{MLCS2K2})$$
$$\Omega_{\rm m} = 0.279 \pm 0.019({\rm stat}) \pm 0.017({\rm syst}) \quad (\texttt{SALT}-\texttt{II})$$

Since we will assume the background evolution is the same as that in the flat $\Lambda$CDM model, the choice of the SNe fitter does not affect our final results significantly, but we should bear in mind that systematic errors are now comparable to statistical errors in SNe observations.

For the Cosmic Microwave Background data in our analysis, we use the WMAP five-year data including the temperature and polarization power spectra [38, 39], and calculate the likelihood using the routine supplied by the WMAP team[1].

### C. Weak lensing

We use the cosmic shear observations from the CFHTLS-Wide third year data release T0003 [11, 35], in which about $2 \times 10^6$ galaxies with $i_{\rm AB}$-magnitudes between 21.5 and 24.5 were imaged on 57 sq. deg. (35 sq. deg. effective area). We use the aperture-mass dispersion $M_{\rm ap}$ [36] following [11, 12]. As in those studies, one can obtain the relevant $\chi^2$ by fitting the theory-predicted aperture-mass dispersion $\langle M^2_{\rm ap}\rangle_{\rm theo}$ given by a model parameter vector $\mathbf{p}$ to $\langle M^2_{\rm ap}\rangle_{\rm obs}$ measured at angular scales $\theta_i$,

$$\chi^2_{\rm Map}(\mathbf{p}) = \sum_{ij} \Big(\big\langle M^2_{\rm ap}(\theta_i)\big\rangle_{\rm obs} - \big\langle M^2_{\rm ap}(\theta_i,\mathbf{p})\big\rangle_{\rm theo}\Big)[\mathbf{C}^{-1}]_{ij} \times \Big(\big\langle M^2_{\rm ap}(\theta_j)\big\rangle_{\rm obs} - \big\langle M^2_{\rm ap}(\theta_j,\mathbf{p})\big\rangle_{\rm theo}\Big). \quad (7)$$

Note that the data covariance matrix $\mathbf{C}$ is the one used in [11] and [12]; it contains shape noise, (non-Gaussian) cosmic variance and residual B-modes [34]. Since it is difficult to model the weak lensing nonlinearity in modified

[1] `http://lambda.gsfc.nasa.gov/`

gravity in a model-independent way [37], we only use the aperture-mass dispersion data measured between 30 and 230 arc min, to remove the strongly nonlinear region from the data. For angles smaller than 30′, the difference between linear and non-linear predictions becomes greater than a factor of two, and we do not wish to suppose that non-linear corrections are reliable on smaller scales.

Theoretically, the aperture-mass dispersion is related to the weak lensing power spectrum via [36]

$$\langle M_{\rm ap}^2\rangle(\theta) = \int \frac{{\rm d}\ell\,\ell}{2\pi} P_\kappa(\ell) \left[\frac{24\,{\rm J}_4(\theta\ell)}{(\theta\ell)^2}\right]^2 , \qquad (8)$$

for the choice of filter in [11]; here, the lensing power spectrum $P_\kappa$ is a projection of the 3D matter-density power spectrum $P_\delta$, weighted by the source galaxy redshift distribution and geometric factors, and ${\rm J}_\alpha(x)$ is the Bessel function of the first kind. To model the redshift distribution of the galaxies, we follow [11] and use the parametrization

$$n(z) \propto \frac{z^a + z^{ab}}{z^b + c}; \quad \int_0^{z_{\rm max}} n(z)\,{\rm d}z = 1\,, \qquad (9)$$

where $\mathcal{N} \supset \{a, b, c\}$ is a set of nuisance parameters to be marginalized over, and we have imposed Gaussian priors on them following [11]: $a = 0.612 \pm 0.043$, $b = 8.125 \pm 0.871$, $c = 0.620 \pm 0.065$. The distribution is normalized by setting $z_{\rm max} = 6$. Then we can calculate the $\chi^2$ for the redshift uncertainty as,

$$\chi_z^2 = \sum_i \frac{[n_i - n(z_i)]^2}{\sigma_i^2}. \qquad (10)$$

where $n_i$ is the normalized number of galaxies in the $i^{\rm th}$ redshift bin and $n(z_i)$ the fitting function, evaluated at the center of the redshift bin. As described in [11], the uncertainty $\sigma_i$ of $n_i$ contains Poisson noise, photo-$z$ error and cosmic variance, and we neglect the cross-correlation between different bins. Then we obtain the $\chi^2$ for weak lensing in the same way as [11],

$$\chi^2_{\rm WL} = \chi^2_{\rm Map} + \chi^2_z\,. \qquad (11)$$

### D. Further priors

Finally, we impose $1\sigma$ Gaussian priors on the Hubble parameter and baryon density of $h = 0.742 \pm 0.036$ and $\Omega_b h^2 = 0.022 \pm 0.002$ from the measurements of Hubble Space Telescope (HST) [40] and Big Bang Nucleosynthesis [41] respectively, and a top hat prior on the cosmic age of 10 Gyr $< t_0 <$ 20 Gyr. The total likelihood is taken to be the product of the separate likelihoods $\mathcal{L}$ of each dataset we used; thus the total $\chi^2$ is the sum of separate $\chi^2$ from individual observations plus that from the priors if we define $\chi^2 \equiv -2\log\mathcal{L}$.

## III. THE PARAMETRIZATION OF MODIFIED GROWTH

In order to test gravity against the growth of cosmological perturbations in a model-independent way, one needs a generalized set of equations to evolve linear perturbations without assuming GR. We work within the framework of the Boltzmann integrator `MGCAMB` [25] [2], which is a variant of `CAMB` [45] [3]. This is based on a system of equations that allows for a general modification of gravity at linear order in the perturbations, while respecting the consistency of the dynamics of long-wavelength perturbations with the background expansion [43, 44]. An interested reader can find a detailed discussion of the equations used in `MGCAMB` and their comparison with other methods in the literature in [26].

We consider scalar metric perturbations about a FRW background for which the line element in the conformal Newtonian gauge reads

$$ds^2 = -a^2(\tau)\left[(1+2\Psi)\,d\tau^2 - (1-2\Phi)\,d\vec{x}^2\right] , \qquad (12)$$

where $\Phi$ and $\Psi$ are functions of time and space. We assume adiabatic initial conditions and covariant conservation of the energy-momentum tensor of matter. The matter conservation at linear order provides two equations which in Fourier space can be written as

$$\delta' + \frac{k}{aH}v - 3\Phi' = 0, \qquad (13)$$

$$v' + v - \frac{k}{aH}\Psi = 0\,, \qquad (14)$$

where $\delta$ is the energy density contrast, $v$ the irrotational component of the peculiar velocity, and primes indicate derivatives with respect to $\ln a$. In order to solve for the evolution of the four scalar perturbations $\{\delta, v, \Phi, \Psi\}$, we need two additional equations, provided by a theory of gravity (such as GR), which specify how the metric perturbations relate to each other, and how they are sourced by the perturbations of the energy-momentum tensor. One can parametrize these relations as

$$\frac{\Phi}{\Psi} = \eta(a,k), \qquad (15)$$

$$k^2\Psi = -4\pi G a^2 \mu(a,k)\rho\Delta\,, \qquad (16)$$

where $\Delta$ is the gauge-invariant comoving density contrast defined as

$$\Delta \equiv \delta + 3\frac{aH}{k}v\,; \qquad (17)$$

$\eta(a,k) = \mu(a,k) = 1$ in GR, while in an alternative model $\mu$ and $\eta$ can in general be functions of both time and scale [24, 25, 42].

[2] `http://userweb.port.ac.uk/~zhaog/MGCAMB.html`
[3] `http://camb.info/`

Defining $\mu$ and $\eta$ in this particular way makes Eqs. (13)-(16) consistent on all linear scales. As shown in [26], on super-horizon scales $\mu$ naturally becomes irrelevant and we are left with only one function, $\eta$, as expected from the super-horizon consistency conditions [43, 44]. Also, having $\mu$ defined through the Poisson equation involving $\Delta$, as opposed to $\delta$, allows for $\mu$ to be equal to unity on all scales for GR.

From $\{\eta,\ \mu\}$, we can derive other parameters which may be more suitable for interpreting observational constraints. For example, since we are using WL and ISW observations in this paper, we will be essentially measuring the power spectra of the lensing potential $(\Phi+\Psi)$ and its time derivative. On the other hand, $\eta$ is not probed directly by any observable and would be highly degenerate with $\mu$, as also pointed out by [32]. For that reason, in addition to $\{\eta,\ \mu\}$, we also present our results in terms of another function, $\Sigma$, defined as

$$\Sigma(a,k) \equiv -\frac{k^2(\Psi+\Phi)}{8\pi G\rho a^2\Delta} = \frac{\mu(1+\eta)}{2}\,. \tag{18}$$

Note that specifying $\mu$ and $\Sigma$ is equivalent to working with $\mu$ and $\eta$. We use both parametrizations to discuss the physics and to interpret our final results.

Since we are interested in testing GR at late times, we assume $\mu(a,k) = \eta(a,k) = 1$ at early times, namely, for $z > z_s$ where $z_s$ denotes the threshold redshift. This is natural in the existing models of modified gravity that aim to explain the late-time acceleration, where departures from GR occur at around the present day horizon scale. Also, the success in explaining the BBN and CMB physics relies on GR being valid at high redshifts.

One could assume a functional parametrization for $\mu$ and $\eta$, either motivated by a modified growth (MG) theory or by simplicity, and fit the parameters to the data [25, 32, 46]. We adopt a different approach, and pixelize $\mu(a,k)$ and $\eta(a,k)$ on a grid in time and scale, fitting their values in each grid point to the data. We then solve the eigenvalue problem for the covariance of the pixels (i.e. perform a PCA) to find their independent linear combinations that can be compared with their prediction in GR [30]. As we will elaborate later, the PCA method has several advantages, such as being model-independent and degeneracy-free, although it is much more computationally expensive. In this work, we will utilize both functional fit and PCA strategies in order to search for any imprint of modified gravity.

To begin with, we parametrize our Universe using:

$$\mathbf{P} \equiv (\omega_b, \omega_c, \Theta_s, \tau, n_s, A_s, \mathcal{N}, \mathcal{X}) \tag{19}$$

where $\omega_b \equiv \Omega_b h^2$ and $\omega_c \equiv \Omega_c h^2$ are the physical baryon and cold dark matter densities relative to the critical density respectively, $\Theta_s$ is the ratio (multiplied by 100) of the sound horizon to the angular diameter distance at decoupling, $\tau$ denotes the optical depth to re-ionization, and $n_s, A_s$ are the primordial power spectrum index and amplitude, respectively. We also vary and marginalize over several nuisance parameters denoted by $\mathcal{N}$ when performing the likelihood analysis for weak lensing and SNe, as we will elaborate later. The modification of gravity is encoded in $\mathcal{X}$, and we consider two different kinds of MG parametrizations, $\mathcal{X}_I$ and $\mathcal{X}_{II}$, as described in the following subsections. Finally, we assume a flat Universe and an effective dark energy equation of state $w = -1$ throughout the expansion history.

### A. A single high redshift transition in $\mu$ and $\eta$: $\mathcal{X}_{\rm I} = \{\mu_0, \eta_0, \Delta z\}$

There is no physical reason to assume that departures from GR ought to be scale-independent, and a PCA forecast analysis [30] actually showed that the scale-dependence of $\mu$ and $\eta$ is better constrained than their average values or the time-dependence. Nevertheless, we shall first consider the case in which $\mu$ and $\eta$ are taken to be scale-independent and transit from their GR values to another constant value below a threshold redshift $z_s$. Aside from simplicity, this will allow an insightful comparison with the results of the scale-dependent analysis later.

To model the time evolution of $\mu$ and $\eta$ we use the hyperbolic tangent function to describe the transition from unity to the constants $\mu_0$ and $\eta_0$ as

$$\begin{aligned}\mu(z) &= \frac{1-\mu_0}{2}\left(1+\tanh\frac{z-z_s}{\Delta z}\right)+\mu_0\ ,\\ \eta(z) &= \frac{1-\eta_0}{2}\left(1+\tanh\frac{z-z_s}{\Delta z}\right)+\eta_0\ .\end{aligned} \tag{20}$$

For a given $z_s$, the above parametrization has three free parameters: $\mu_0, \eta_0$ and $\Delta z$. In Figs. 1 and 2, we show the imprints of MG on the weak lensing aperture-mass dispersion (see details in Sec. II C) and CMB TT power spectra for different values of the MG parameters respectively. To be more physically transparent, we will also present our results in terms of the $\{\mu,\ \Sigma\}$ parametrization (see Eq. (18)).

We find that both WL and CMB observables are more sensitive to the variation of $\Sigma_0$ than to that of $\mu_0$ for both the $z_s = 1$ and the $z_s = 2$ case. This is expected since WL and CMB (via the ISW effect) measure, respectively, the power spectra of $(\Phi+\Psi)$ and their time derivative, and are primarily controlled by $\Sigma_0$. However, at late times on sub-horizon scales, $\mu_0$ only affects $(\Phi+\Psi)$ indirectly by altering the growth rate of $\Delta$ via

$$\ddot{\Delta} + \mathcal{H}\dot{\Delta} - 4\pi G\rho a^2\mu_0\Delta = 0\,, \tag{21}$$

where the over-dot represents differentiation with respect to the conformal time, and $\mathcal{H} \equiv \dot{a}/a$ is the conformal Hubble parameter. Therefore changing $(\Phi+\Psi)$ by varying $\mu_0$ is much less efficient than tuning the multiplier $\Sigma_0$. This can be seen in panels $(C_1, C_2)$, where we plot the relative difference of the evolution of $\Delta$ with respect to GR for different values of $\mu_0$. One can read from the

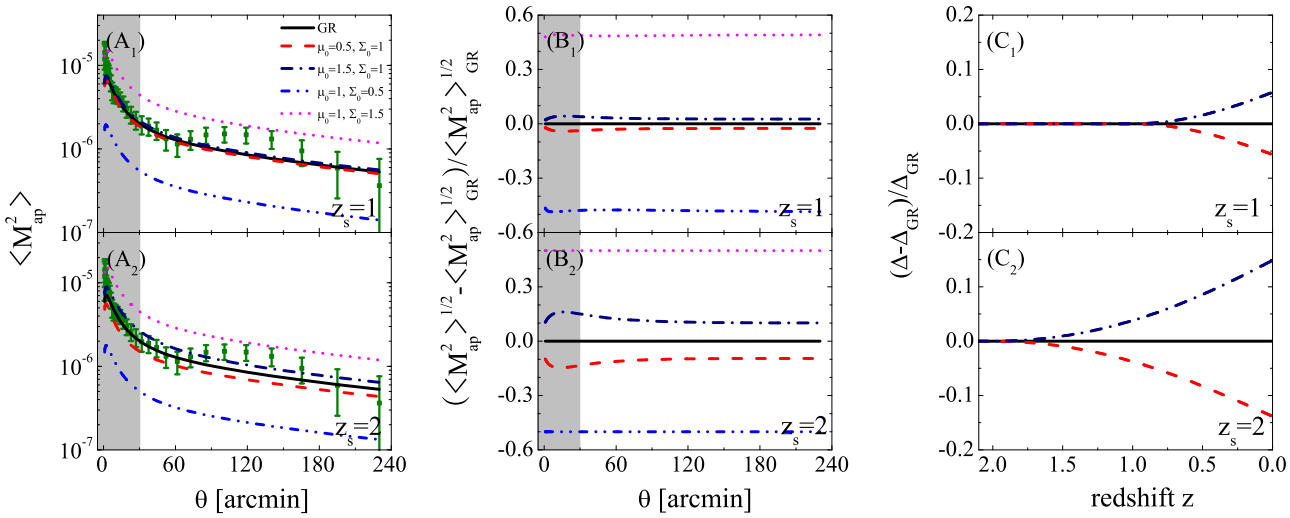


FIG. 1: Imprints of modified gravity parametrized by $\mathcal{X}_{\rm I}$ on the weak lensing aperture mass dispersion (panels $A_1, A_2$), relative difference in $M_{\rm ap}^{1/2}$ with respect to GR ($B_1, B_2$), and relative difference in $\Delta$ with respect to GR ($C_1, C_2$). The model parameters are shown in the legend of panel ($A_1$). The shaded regions in panels ($A_1, A_2, B_1, B_2$) are excluded from our analysis. The data with error bars over-plotted in panels ($A_1, A_2$) are taken from the CFHTLS survey.

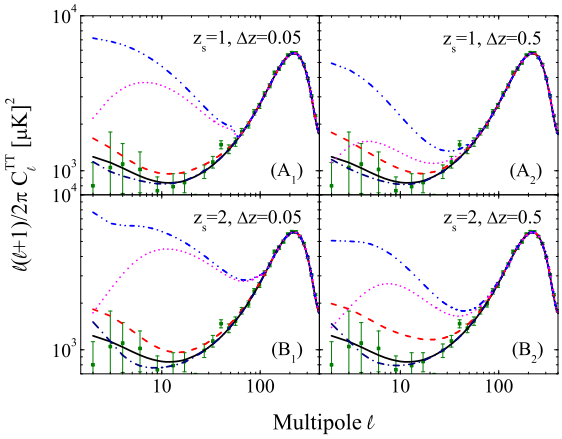


FIG. 2: Imprints of modified gravity parametrized by $\mathcal{X}_{\rm I}$ on the CMB TT power spectra for different threshold redshift $z_s$ and different transition width $\Delta z$. Different models are distinguished by different line styles and colors, as shown in panel ($A_1$) of Fig. 1. The data points with error bars are taken from the WMAP 5-year survey.

plot that, for example in the case $z_s = 2$, if one fixes $\Sigma_0 = 1$ and increases $\mu_0$ by 50%, $\Delta$ is enhanced by 15% at $z = 0$. From this, it follows from Eq. (18) that $(\Phi + \Psi)$ is also enhanced by 15% at $z = 0$. Finally $M_{\rm ap}^{1/2}$ should be enhanced by roughly the same amount according to Eq. (8), and this is what we see in panel ($B_2$) (navy dashed-dotted line). On the other hand, if $\mu_0$ is fixed to unity and $\Sigma_0$ is enhanced by 50%, then Eq. (18) clearly shows that $(\Phi+\Psi)$ and $M_{\rm ap}^{1/2}$ should be enhanced by 50% as well, as shown in panel ($B_2$) (magenta short-dashed line). Therefore we can conclude that our observables are more sensitive to $\Sigma_0$ than $\mu_0$ for both cases of the transition redshift, $z_s = 1$ and $z_s = 2$.

When varying the growth rate controller $\mu_0$, the earlier the redshift at which it is turned on, the more total change in growth and gravitational potential will be accumulated by the present day, as shown in panels ($C_1, C_2$). Thus our observables are more sensitive to the same amount of variation in the MG parameters in the case of $z_s = 2$ compared to $z_s = 1$ due to this "accumulation effect".

In Fig. 2, we see that the CMB angular spectrum will strongly disfavor a sharp transition in $\Sigma$. This is obvious from Eq. (18) — a sharp transition in $\Sigma$ triggers a sudden change in $(\Phi + \Psi)$, making $(\dot{\Phi} + \dot{\Psi})$ diverge around the transition region, and this is what we see in panels ($A_1, B_1$). Note that if the transition width $\Delta z$ is small enough, the ISW signal in the CMB spectrum converges because the details of the transition become irrelevant in the $\Delta z \to 0$ limit; then the ISW signal is determined solely by the change of $(\Phi + \Psi)$ and the window function at the transition. We find that the choice $\Delta z = 0.05$ is narrow enough to approximate well to this $\Delta z \to 0$ limit. We also show the results for a milder transition, namely, $\Delta z = 0.5$ in panels ($A_2, B_2$) of Fig. 2. We see that the $\mu_0$ curves are largely unchanged, implying that the effect of varying $\mu_0$ is not sensitive to $\Delta z$. However, the 'bumps'

on the $\Sigma_0$ curves become less pronounced for smoother transitions, as expected. In the following analysis, we will show results corresponding to the parametrization $\mathcal{X}_{\rm I}$ for both fixed $\Delta z = 0.05$, and a floating $\Delta z$, which will then be treated as a nuisance parameter and marginalized over.

### B. Pixellation + PCA: $\mathcal{X}_{\rm II} = \{\mu_i, \Sigma_i, (i = 1..4)\}$

Even though the parametrization $\mathcal{X}_{\rm I}$ has the advantage of simplicity, it is not theoretically well-motivated. Models of modified gravity commonly introduce a scale into the theory, and correspondingly $\mu$ and $\eta$ always have some scale dependence. Moreover, this parametrization is not phenomenologically efficient to capture a deviation from GR. As shown in [30], the growth observables are much more sensitive to the scale dependence of the two functions, than to their time dependence.

In order to be more general, one can pixelize $\mu$ and $\eta$ in the $(k, z)$ plane and treat their values on each grid point as free parameters. These parameters are in general correlated with each other, and this blurs the interpretation if one attempts to constrain them directly. Instead, one can construct new variables that are uncorrelated linear combinations of the original parameters and use them to test GR. This can be achieved by diagonalizing the covariance matrix of the original pixels and using the de-correlation matrix to map the original pixels onto the uncorrelated variables. Such de-correlation, or PCA, has been used to study constraints on the evolution of the dark energy equation of state $w(z)$ [47–49]. Here we employ a two-dimensional PCA in the $(k, z)$ plane since $\mu$ and $\eta$ are functions of time and scale.

The model-dependence disappears in the limit of a very fine tessellation of the two functions into pixels. In reality, computing costs limit the number of pixels one can afford to fit. To determine the optimal number of pixels, we performed a Fisher Matrix PCA forecast, analogous to the one in [30], finding that in order to capture the $(k, z)$ dependence of the best constrained combined eigenmodes one needs at least a $2 \times 2$ pixels for $\mu$ and $\Sigma$ in the range of $k \in [0, 0.2], z \in [0, 2]$, as illustrated in panel A of Fig. 7. Note that here we choose to work with the $\{\mu, \Sigma\}$ parametrization because the ISW and WL constrain $\Sigma$ more directly than $\eta$. We have checked that our results do not change if we pixelize $\{\mu, \eta\}$ instead. To properly set the transition width between the neighboring pixels, we start from a wide transition width ($\Delta z = 0.5$), and reduce it until the final results converge. As in the case of parametrization $\mathcal{X}_{\rm I}$, we found convergent results when $\Delta z \lesssim 0.05$, therefore we chose $\Delta z = 0.05$ for the transition width.

Thus, in model $\mathcal{X}_{\rm II}$, we start by fitting 8 pixels, $\{\mu_i, \Sigma_i, (i = 1..4)\}$, along with the non-MG parameters, to obtain the covariance matrix of all parameters. We then diagonalize the $8 \times 8$ block of the covariance matrix, $C_{(\mu,\Sigma)}$ corresponding to $\mu$ and $\Sigma$:

$$C_{(\mu,\Sigma)} = W \Lambda^{-1} W^T \,. \tag{22}$$

The rows of the de-correlation matrix $W$ are the principal components [50], or eigenmodes, while the diagonal elements of $\Lambda$, i.e. the eigenvalues, are the inverses of the variances on the uncorrelated linear combinations of the original pixels. Namely, we use $W$ to rotate the original parameters, denoted by the vector $\mathbf{p}$, into new uncorrelated parameters $\mathbf{q}$ defined as

$$q_i = -1 + \sum_j W_{ij} p_j / \sum_j W_{ij} \,. \tag{23}$$

In GR one has $\mathbf{q} = \mathbf{0}$, since $\mathbf{p} = \mathbf{1}$, therefore we can test GR by performing a null test on $\mathbf{q}$. By construction, the eigenvectors are orthogonal and the $q$'s have uncorrelated errors given by the inverses of the eigenvalues.

## IV. RESULTS

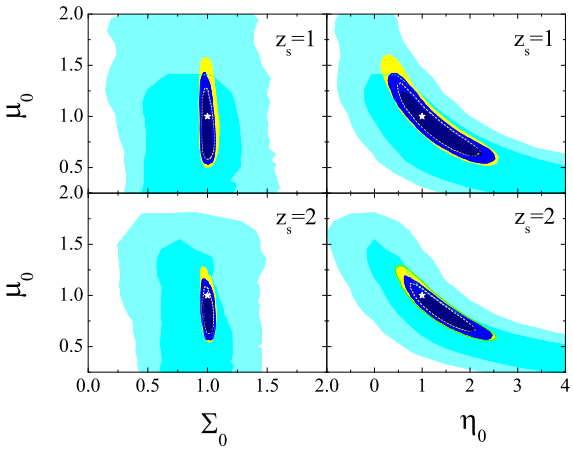


FIG. 3: 68% and 95% C.L. contour plots for $\{\mu_0,\ \eta_0\}$ and $\{\mu_0,\ \Sigma_0\}$ for two different threshold redshifts: $z_s = 1$ (upper panels) and $z_s = 2$ (lower panels). In both cases the transition width is fixed to $\Delta z = 0.05$. From outside in, the shaded regions in cyan, yellow and blue illustrate the contours derived from the data of CFHTLS+CMB shift parameters, CFHTLS+WMAP5 and CFHTLS+WMAP5+ISW, respectively. For the contours shaded in the same color, the light and dark regions show the 68% and 95% C.L. contour respectively. In all cases, the SNe data are combined, and the priors of cosmic age, BBN and HST are applied. The star denotes the GR values.

Given the set of cosmological parameters $\mathbf{P}$ in Eq. (19), we calculate the observables, which include the CMB temperature and polarization spectra, the CMB/galaxy cross-correlation (which we often refer to as ISW), the luminosity distance for SNe, and the WL aperture-mass

TABLE I: The mean values of $\mu_0$, $\eta_0$ and $\Sigma_0$ with 68% and 95% C.L. error bars for different models and for different data combinations. Note that '$\ell_A, R$','CMB', 'ISW' and 'WL' are short-hands for WMAP5 shift parameters, full WMAP5 data, ISW data and CFHTLS data explained in the text, respectively.

| | | $z_s = 1$ | | | $z_s = 2$ | | |
|---|---|---|---|---|---|---|---|
| | | $\mu_0$ | $\eta_0$ | $\Sigma_0$ | $\mu_0$ | $\eta_0$ | $\Sigma_0$ |
| $\Delta z$ fixed | CMB | $1.0^{+0.11+0.40}_{-0.13-0.34}$ | $1.1^{+0.51+1.0}_{-0.48-0.74}$ | $1.0 \pm 0.03 \pm 0.06$ | $1.1^{+0.16+0.37}_{-0.17-0.31}$ | $0.96^{+0.11+0.62}_{-0.18-0.47}$ | $1.0 \pm 0.025 \pm 0.05$ |
| | CMB+ISW | $0.97^{+0.09+0.37}_{-0.13-0.29}$ | $1.2 \pm 0.50^{+0.94}_{-0.77}$ | $1.1 \pm 0.028 \pm 0.055$ | $1.0^{+0.15+0.35}_{-0.16-0.28}$ | $0.98^{+0.10+0.55}_{-0.17-0.45}$ | $1.0 \pm 0.024 \pm 0.05$ |
| | WL+$\ell_A, R$ | $0.63^{+0.65+1.36}_{-0.45-0.57}$ | $1.7^{+3.2+6.2}_{-1.6-2.3}$ | $0.86 \pm 0.39 \pm 0.74$ | $0.58^{+0.92+1.17}_{-0.38-0.55}$ | $2.1^{+3.0+5.7}_{-1.5-2.2}$ | $0.89 \pm 0.19 \pm 0.33$ |
| | WL+CMB | $0.95 \pm 0.24^{+0.54}_{-0.34}$ | $1.2 \pm 0.60^{+1.1}_{-0.91}$ | $1.0 \pm 0.033^{+0.07}_{-0.06}$ | $0.87 \pm 0.15^{+0.33}_{-0.25}$ | $1.4 \pm 0.44^{+0.91}_{-0.76}$ | $1.0 \pm 0.03 \pm 0.05$ |
| | WL+CMB+ISW | $0.90 \pm 0.21^{+0.42}_{-0.29}$ | $1.3 \pm 0.56^{+0.98}_{-0.84}$ | $1.0 \pm 0.027 \pm 0.05$ | $0.84 \pm 0.13^{+0.27}_{-0.21}$ | $1.4 \pm 0.39^{+0.81}_{-0.69}$ | $1.0 \pm 0.025 \pm 0.05$ |
| $\Delta z$ float | WL+CMB+ISW | $1.1^{+0.62+0.80}_{-0.34-0.45}$ | $0.98^{+0.73+1.2}_{-1.0-1.4}$ | $0.94^{+0.08+0.12}_{-0.14-0.32}$ | $0.87 \pm 0.12^{+0.24}_{-0.19}$ | $1.3 \pm 0.35^{+0.65}_{-0.60}$ | $1.0 \pm 0.03 \pm 0.06$ |

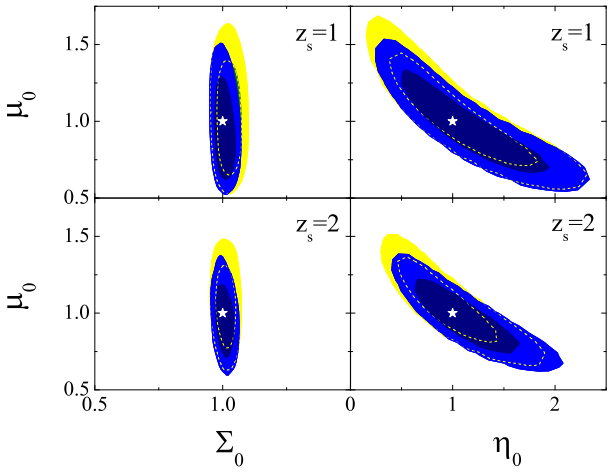


FIG. 4: 68% and 95% C.L. contour plots for $\{\mu_0,\ \eta_0\}$ and $\{\mu_0,\ \Sigma_0\}$ for two different threshold redshifts: $z_s = 1$ (upper panels) and $z_s = 2$ (lower panels). In both cases the transition width is fixed to $\Delta z = 0.05$. From outside in, the shaded regions in yellow and blue illustrate the contours derived from the data of WMAP5 and WMAP5+ISW, respectively. For the contours shaded in the same color, the light and dark regions show the 68% and 95% C.L. contour respectively. In all cases, the SNe data are combined, and the priors of cosmic age, BBN and HST are applied. The star denotes the GR values.

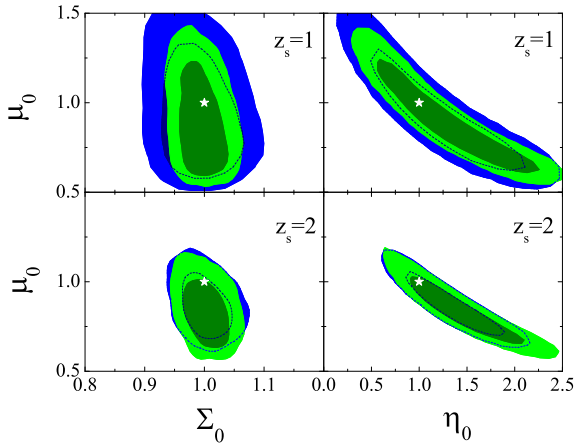


FIG. 5: 68% (dark shaded) and 95% C.L. (light shaded) contour plots for $\{\mu_0, \Sigma_0\}$ and $\{\mu_0, \eta_0\}$ for two different threshold redshifts: $z_s = 1$ (upper panels) and $z_s = 2$ (lower panels). All the constraints are from the combined data of ISW, WMAP5 and CFHTLS. To obtain the front, green contours, the transition width is fixed to $\Delta z = 0.05$, while the blue contours on the back layers show the case of a floating $\Delta z$, which is marginalized over. The dashed curves show the covered contour edges. The star illustrates the GR values.

dispersion $M_{\rm ap}$, using `MGCAMB`. We then fit the available CMB, ISW, SNe and WL to observations using a modified version of the Markov Chain Monte Carlo (MCMC) package `CosmoMC` [4] [51], based on Bayesian statistics. Our main results are summarized in Figs. 3-10 and Tables I -IV.

[4] `http://cosmologist.info/cosmomc/`

### A. Parametrization $\mathcal{X}_{\rm I}$

Let us start with the single-transition parametrization $\mathcal{X}_{\rm I}$ of the MG parameters. In Fig. 3, we show the 68% and 95% C.L. contours of $\{\mu_0,\ \eta_0\}$ and $\{\mu_0,\ \Sigma_0\}$ for the cases of $z_s = 1$ (upper panels) and $z_s = 2$ (lower panels) for different data combinations. Here the transition width is fixed to $\Delta z = 0.05$. We show contours derived from the CFHTLS data combined with the CMB shift parameters $\ell_A$ and $R$ given in [38], CFHTLS plus full WMAP5 and CFHTLS+WMAP5+ISW. In Fig. 4, we also show contours derived from full WMAP5 and WMAP5 + ISW. All cases include the SNe data, and the cosmic age, BBN and HST priors.

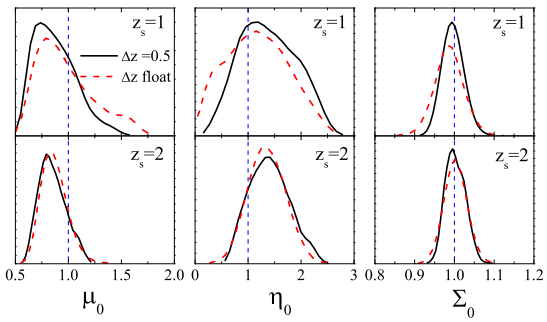


FIG. 6: 1-D posterior distributions of $\mu_0, \eta_0$, and $\Sigma_0$ derived from the joint analysis of ISW, WMAP5 and CFHTLS data. The black solid lines show the cases of sharp transition, i.e., $\Delta z = 0.05$, while the red dashed lines illustrated the cases where $\Delta z$ varies and is marginalized over. The upper and lower panels are for the $z_s = 1$ and $z_s = 2$ cases, respectively. The vertical dashed lines illustrate $\mu_0 = \eta_0 = \Sigma_0 = 1$ to guide eyes.

One thing that can be noticed from Figs. 3 and 4 is that the $z_s = 2$ models, shown in the lower panels, are in general better constrained than the $z_s = 1$ ones, shown in the upper panels. This is due to the 'accumulation effect' explained in Sec. III A.

In Fig. 3, the largest cyan contours show that the CFHTLS WL data combined with CMB shift parameters are able to constrain $\Sigma_0$ at $\sim 20\%$ level, but only weakly constrain $\mu_0$ and $\eta_0$, since WL observables are directly sensitive to the variation in $\Sigma_0$ as explained in Sec. III A. For the same reason, one sees little degeneracy in the $\{\Sigma_0,\ \mu_0\}$ plane. However, in the $\{\mu_0,\ \eta_0\}$ plane, the contours show a banana shape, which indicates that $\mu_0$ strongly anti-correlates with $\eta_0$. This is understandable — one can increase $\mu_0$ to enhance growth and thus $\Psi$, but then $\eta_0$ can be lowered to decrease $\Phi$, leaving $\Phi + \Psi$ unchanged. Also, as discussed in Sec. III A, the sensitivity of the observables to $\mu_0$ is comparable to their sensitivity to $\eta_0$, although the former is slightly larger than the latter. This is the reason why the degeneracy is visible. From Table I, we see that CFHTLS combined with CMB shift parameters favor slightly lower values of $\mu_0$ and $\Sigma_0$ than unity, but GR is still within the $1\sigma$ level.

The constraints become much tighter if one includes the full WMAP5 data, as shown in the yellow contours in Figs. 3 and 4. This is mainly because the WMAP5 ISW-ISW ACFs strongly penalize abrupt changes in $\Sigma_0$, as we show in Fig. 2. The constraints get even tighter when the ISW-gal CCFs data are added, as illustrated in the innermost blue contours. From Fig. 3 and Table I we see that for the case of $z_s = 1$ GR is fully consistent with the combined data. For the $z_s = 2$ case, GR is also consistent, but is on the $1\sigma$ edge, indicating that a model with a lower $\mu_0$ would be slightly favored when WL data are included. GR is always closer to the best-fit model when WL data are not used, as we can see in Fig. 4.

If the transition width $\Delta z$ is allowed to vary in the range of $[0.05, 0.5]$ one could expect a dilution of the constraints. We observe the result in Figs. 5 and 6, which show the contours and 1-D posterior distributions for MG parameters for the cases of sharp transitions and floating transitions for all the data combined. As we can see, marginalizing over a floating $\Delta z$ degrades the constraints on $\mu_0, \eta_0$ and $\Sigma_0$ by roughly 150%, 50% and 300%, respectively for the $z_s = 1$ case, but there is little degradation for the $z_s = 2$ case. Again, we see that GR is a perfect fit in the $z_s = 1$ case, while a model with a lower $\mu_0$ is slightly favored in the $z_s = 2$ case when all data are combined.

This can be understood as follows. As shown in panels $(A_1, B_1)$ in Fig. 2, for the $z_s = 1$ case, a sharp transition in $\Sigma$ produces a huge bump on CMB TT spectrum at $\ell \lesssim 70$, where the cosmic variance dominates the error budget. If the transition is mild, the bump structure becomes less pronounced as shown in panel $A_2$, thus there is less tension with the CMB data, which in turn loosens the constraints on the MG parameters. However, for the $z_s = 2$ case, the bump appears at $\ell \lesssim 150$ on the CMB spectrum, where WMAP5 has precise measurements. It is true that relaxing $\Delta z$ reduces the bump feature somewhat as illustrated in panel $B_2$; however the constraints on the MG parameters cannot be diluted to a large extent due to the high quality CMB data at $70 \lesssim \ell \lesssim 150$.

Note that the constraint on $\Sigma$ from the ISW effect is much tighter than the current WL constraints, due to the sensitivity of the ISW to the gravitational transition. This means that the ISW data provide valuable information on the time evolution of modified gravity parameters.

### B. Parametrization $\mathcal{X}_{\rm II}$

We present results for the second parametrization $\mathcal{X}_{\rm II}$ with and without the inclusion of WL data, as summarized in Figs. 7, 10 and Tables II, IV respectively. Starting from the analysis based on the full data set, in panel (A) of Fig. 7, we show our $\Sigma$ and $\mu$ pixellation, and in panel (B), we show the 1-D posterior distributions of the eight $\Sigma$ and $\mu$ pixels. As we found for the parametrization $\mathcal{X}_{\rm I}$, the $\Sigma$ pixels are in general better constrained than the $\mu$ pixels. We find that the constraints on all the pixels are consistent with the GR prediction except for that of $\Sigma_3$, which is $\Sigma_3 = 0.80 \pm 0.12 \pm 0.22$ (mean value with 68% and 95% C.L. errors). This means that $\Sigma_3$ deviates from the GR prediction at an almost $2\sigma$ level. However, the correlation among all of the eight pixels blurs the naïve interpretation of the seemingly $2\sigma$ signal. Thus, we follow the PCA prescription explained in Sec. III B and obtain the linearly uncorrelated parameters, $q$'s, using Eq. (23).

The three best constrained eigenmodes are shown in panel $(C)$ of Fig. 7 and are fairly well-localized. One can clearly see that they primarily depend on the $\Sigma$ pixels, which are expected to be better measured by the ISW

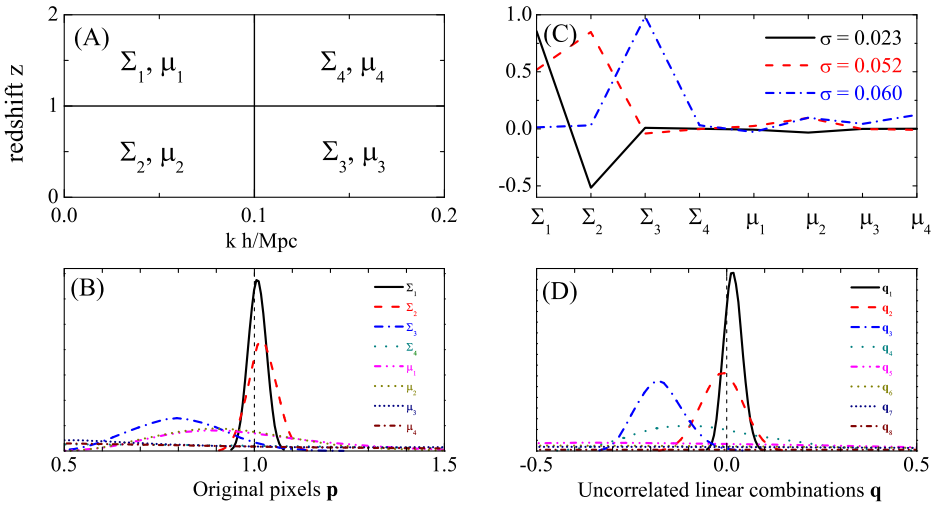


FIG. 7: Panel (A): the $\Sigma, \mu$ pixellation used in this work; Panels (B) and (D): the 1-D posterior distributions of $\mathbf{p}$ and $\mathbf{q}$, which denote the original pixels of $\Sigma$ and $\mu$, and the uncorrelated linear combinations of the original pixels, respectively. The likelihood distributions are normalized so that the area of each distribution is unity; Panel (C): the first three eigenfunctions, i.e. values of $\mathbf{W}$ relating $\mathbf{p}$ and $\mathbf{q}$ via Eq. (23). These are derived from the joint analysis of ISW, WMAP5 and CFHTLS data.

TABLE II: Mean values, and 68% and 95% C.L. constraints of the original pixels (left panel) and the uncorrelated linear combinations of the pixels (right panel). All data sets are used.

| | | | |
|---|---|---|---|
| $\Sigma_1$ | $1.0 \pm 0.02 \pm 0.04$ | $q_1$ | $0.0 \pm 0.02 \pm 0.04$ |
| $\Sigma_2$ | $1.0 \pm 0.04 \pm 0.07$ | $q_2$ | $0.0 \pm 0.05 \pm 0.10$ |
| $\Sigma_3$ | $0.80 \pm 0.12 \pm 0.22$ | $q_3$ | $-0.17 \pm 0.06^{+0.13}_{-0.11}$ |
| $\Sigma_4$ | $0.83^{+0.63+1.4}_{-0.60-0.83}$ | $q_4$ | $-0.05 \pm 0.17^{+0.37}_{-0.28}$ |
| $\mu_1$ | $0.96 \pm 0.20^{+0.46}_{-0.32}$ | $q_5$ | $-0.10 \pm 0.52^{+1.1}_{-0.81}$ |
| $\mu_2$ | $0.94 \pm 0.18^{+0.40}_{-0.29}$ | $q_6$ | $-0.17 \pm 0.79^{+1.7}_{-1.2}$ |
| $\mu_3$ | $0.94^{+0.64+1.3}_{-0.52-0.70}$ | $q_7$ | $-0.02^{+1.1+2.1}_{-1.0-2.0}$ |
| $\mu_4$ | $0.86^{+0.69+1.6}_{-0.62-0.81}$ | $q_8$ | $-0.25 \pm 3.2^{+6.0}_{-5.2}$ |

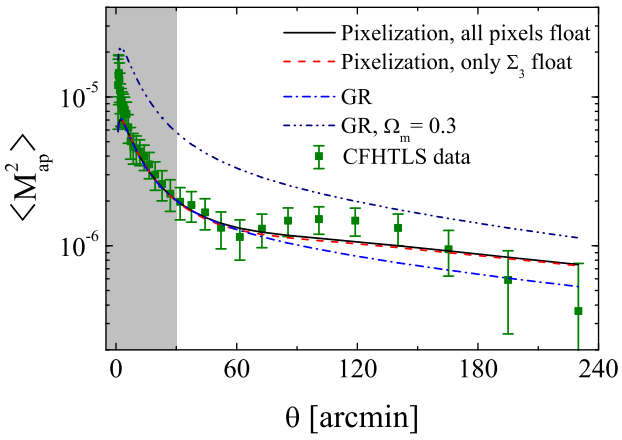


FIG. 8: Best-fit aperture mass power spectra $\langle M^2_{\rm ap} \rangle$ for different MG parametrizations shown in different colors and line styles. Black solid: parametrization $\mathcal{X}_{\rm II}$ with all the pixels varying; Red dashed: parametrization $\mathcal{X}_{\rm II}$ with only $\Sigma_3$ varying; Blue dashed-dotted: GR; Navy dashed-dotted-dotted: GR with a fixed $\Omega_m = 0.3$. The data points with error bars show the CFHTLS data; the shaded region is excluded from our analysis.

and WL. In particular, the eigenmode corresponding to $q_i$ ($i \leq 3$) received the largest contribution from $\Sigma_i$ ($i \leq 3$). From the eigenmodes we can deduce the following relations between the $q's$ and the original pixels:

$$q_1 \approx -1 + \frac{0.85\Sigma_1 - 0.52\Sigma_2}{0.85 - 0.52} = 0.0 \pm 0.02 \pm 0.04$$
$$q_2 \approx -1 + \frac{0.52\Sigma_1 + 0.85\Sigma_2}{0.52 + 0.85} = 0.0 \pm 0.05 \pm 0.10$$
$$q_3 \approx -1 + \Sigma_3 = -0.17 \pm 0.06^{+0.13}_{-0.11}\,. \qquad (24)$$

Namely, $\Sigma_1$ is strongly degenerate with $\Sigma_2$, while $\Sigma_3$ is largely independent of $\Sigma_1$ or $\Sigma_2$;

One can understand this by realizing that the current ISW data can put stronger constraints on the MG parameters than the current WL data, due to the sensitivity of the ISW to any modification of growth at $z \lesssim 2$. Future WL surveys (including the upcoming final results from the full CFHTLS survey) will feature higher signal-to-noise and will provide tighter limits on MG parameters [30]; however, at present, the ISW component dominates in our data combination, making the linear combinations of the $\Sigma$ pixels on large scales ($k \lesssim 0.1$h/Mpc),

TABLE III: The relative improvement on $\chi^2$ with respect to the ΛCDM model for different models. The $\Delta\chi^2$ is shown for different data separately. The mean values with 68% and 95% C.L. error bars of constraints on $\Omega_{\rm m}$ and $\sigma_8$ are also shown.

| | $\Delta\chi^2_{\rm WL}$ | $\Delta\chi^2_{\rm CMB}$ | $\Delta\chi^2_{\rm ISW}$ | $\Delta\chi^2_{\rm SN}$ | $\Delta\chi^2_{\rm ToT}$ | $\Omega_{\rm m}$ | $\sigma_8$ |
|---|---|---|---|---|---|---|---|
| ΛCDM | 0 | 0 | 0 | 0 | 0 | $0.244 \pm 0.004$ | $0.765 \pm 0.006$ |
| $\mathcal{X} = \mathcal{X}_{\rm I},\ z_s = 1,\ \Delta z = 0.05$ | −0.65 | +0.11 | −0.10 | −0.17 | −0.81 | $0.252 \pm 0.008$ | $0.74 \pm 0.02$ |
| $\mathcal{X} = \mathcal{X}_{\rm I},\ z_s = 1,\ \Delta z$ float | −0.63 | +0.01 | −0.18 | −0.50 | −1.3 | $0.251 \pm 0.008$ | $0.74 \pm 0.02$ |
| $\mathcal{X} = \mathcal{X}_{\rm I},\ z_s = 2,\ \Delta z = 0.05$ | −0.73 | +2.0 | −0.45 | −2.4 | −1.6 | $0.247 \pm 0.006$ | $0.76 \pm 0.02$ |
| $\mathcal{X} = \mathcal{X}_{\rm I},\ z_s = 2,\ \Delta z$ float | −1.4 | +1.8 | −0.44 | −2.6 | −2.6 | $0.255 \pm 0.019$ | $0.79 \pm 0.06$ |
| $\mathcal{X} = \mathcal{X}_{\rm II}$, all pixels float | −2.3 | +4.1 | +1.4 | −12.3 | −9.1 | $0.30 \pm 0.024$ | $0.80 \pm 0.069$ |
| $\mathcal{X} = \mathcal{X}_{\rm II}$, only $\Sigma_3$ float | −2.2 | +5.3 | +0.48 | −12.2 | −8.6 | $0.30 \pm 0.022$ | $0.82 \pm 0.021$ |

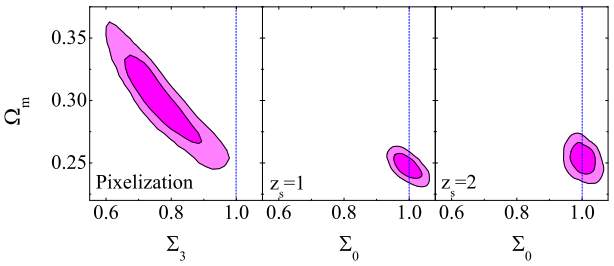


FIG. 9: The 68 and 95% C.L. contour plots of $\{\Omega_{\rm m}, \Sigma_3\}$ (left panel) for parametrization $\mathcal{X}_{\rm II}$, and $\{\Omega_{\rm m}, \Sigma_0\}$ (middle and right panels) for parametrization $\mathcal{X}_{\rm I}$. See text for details.

$\Sigma_1$ and $\Sigma_2$, best measured.

The constraints on the $q$'s are summarized in the right panel of Table II, and the 1-D posterior distributions are shown in panel (D) of Fig. 7. We find that all the $q$'s are consistent with zero as predicted by GR, except for $q_3$, which deviates from the GR prediction at more than 95% confidence level. This means that our measurement of $\Sigma$ and/or $\mu$ deviate from unity at the level of at least 95% C.L. at some point in $(k, z)$.

To spot the source of this signal, we fix all the pixels to unity except for $\Sigma_3$, which we allow to vary. Interestingly, we find that the goodness-of-fit of this one-pixel model is almost identical to that of the 8-pixel model. To be explicit, we list the $\chi^2$ for each dataset separately for both models, and also show the constraints on $\Omega_{\rm m}$ and $\sigma_8$ for these models in Table III. For comparison, we also do the same for the models parametrized using $\mathcal{X}_{\rm I}$. Comparing to ΛCDM, we find that allowing $\Sigma_3$ to vary can reduce the WL $\chi^2$ by 2.2, while also reducing the SNe $\chi^2$ by roughly 12. This $\Sigma_3$CDM model has a best-fit $\Omega_{\rm m}$ of 0.3, which is much larger than 0.24 for ΛCDM. The allowance for a high $\Omega_{\rm m}$ is the reason for the significant SNe data preference for this one-pixel model, since $\Omega_{\rm m} = 0.3$ is the best-fit value for the SNe sample we use [4]. Note that in ΛCDM, $\Omega_{\rm m} = 0.3$ is strongly disfavored by WL data, as we show in Fig. 8 (navy dashed-dotted-dotted line), since there increasing $\Omega_{\rm m}$ shifts the best-fitted $M_{\rm ap}$ (blue dashed-dotted) on all scales, which is in serious disagreement with the data, especially on scales $\theta < 60$ arc min.

The cause of the apparent $2\sigma$ hint of departure from GR can be easily identified. There is a clear "bump" feature in the CFHTLS data (e.g. Fig. 8) at $\theta \simeq 120$ arc min, which can be attributed to a systematic effect [34]: according to the CFHTLS team, this is a known issue, due to residual field-to-field variations in shear estimation on the scale of the camera field-of-view. As an informative exercise, we study how we could improve the fit assuming a cosmological source for the feature. One could shift the curve at $\theta \geq 60$ arc min to follow the "bump" more closely. Such a scale-dependent tweak of $M_{\rm ap}$ can not be realized by tuning the MG parameters in the parametrization $\mathcal{X}_{\rm I}$. However, in the parametrization $\mathcal{X}_{\rm II}$, one can achieve this by firstly increasing $\Omega_{\rm m}$, then lowering the growth rate on small scales ($\theta < 60$ arc min), which can be effectively done by lowering $\Sigma_3$. The resultant fit is shown in Fig. 8 as a red-dashed line, which is almost identical to the best-fit 8-pixel model.

To see this point more clearly, in Fig. 9 we show the contour plots between $\Omega_{\rm m}$ and $\Sigma_3$, and $\Omega_{\rm m}$ and $\Sigma_0$ of $\mathcal{X}_{\rm I}$ for the combined data. As we can see, in the one-pixel ($\Sigma_3$) model can one obtain a high $\Omega_{\rm m}$ as favored by the SNe data, while in parametrization $\mathcal{X}_{\rm I}$, $\Sigma_0$ is tightly constrained, so that a high $\Omega_{\rm m}$ is definitely not allowed. Notice that the CMB and ISW data disfavor a high $\Omega_{\rm m}$, as we see in Table III, but the preference from the WL and SNe data outweighs this penalty, making a lower $\Sigma_3$ and higher $\Omega_{\rm m}$ strongly favored by the combined data. Also, the one-pixel model would be strongly favored by the data from the model-selection point of view, since one can reduce the total $\chi^2$ by 8.6 by introducing one more parameter ($\Sigma_3$) over ΛCDM, even though this model was constructed *a posteriori*.

As stated above, it is likely that the "bump", which is responsible for this $2\sigma$ deviation, is due to a systematic effect [34], which according to the CFHTLS team is due to residual field-to-field variations in shear estimation on the scale of the camera field-of-view; this explains the scale of the bump. On these grounds, we stress again that it is premature to make any statements about the validity

of ΛCDM based on this feature, even though technically we cannot rule out the new physics at this point.

In order to be conservative about this issue, we also perform the $\mathcal{X}_{\rm II}$ analysis without including the WL data from CFHTLS. The results are summarized in Fig. 10 and Table IV. The relation between the uncorrelated parameters $q$'s and the original pixels, and the 68% and 95% C.L. constraints on the $q$'s are now given by

$$q_1 \approx -1 + \frac{0.90\Sigma_1 - 0.44\Sigma_2}{0.90 - 0.44} = 0.0 \pm 0.02 \pm 0.04$$
$$q_2 \approx -1 + \frac{0.44\Sigma_1 + 0.90\Sigma_2}{0.44 + 0.90} = 0.0 \pm 0.04 \pm 0.07$$
$$q_3 \approx -1 + \frac{0.52\mu_1 - 0.85\mu_2}{0.52 - 0.85} = -0.07 \pm 0.17^{+0.36}_{-0.31} \quad (25)$$

As expected, the first two best constrained modes are almost unchanged even if we remove the CFHTLS data, confirming that these modes are mostly constrained by the ISW effect. On the other hand, the bound on $\Sigma_3$ becomes very weak, demonstrating that the CFHTLS data are responsible for the constraint on this parameter. In the current case we find that all the eight uncorrelated parameters are consistent with GR with 95 % C.L.

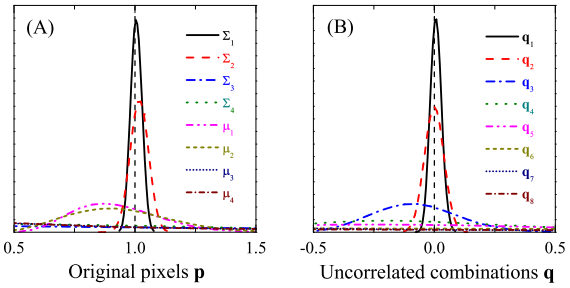


FIG. 10: Panels (A) and (B): The 1-D posterior distributions of $\mathbf{p}$ and $\mathbf{q}$, which denote the original pixels of $\Sigma$ and $\mu$, and the uncorrelated linear combinations of the original pixels, respectively. The likelihood distributions are normalized so that the area of each distribution is unity. These are derived from the joint analysis of ISW and WMAP5 data, without the CFHTLS WL data..

TABLE IV: Mean values, and 68% and 95% C.L. constraints of the original pixels (left panel) and the uncorrelated linear combinations of the pixels (right panel). Results without the CFHTLS WL data.

| | | | |
|---|---|---|---|
| $\Sigma_1$ | $1.0 \pm 0.02 \pm 0.04$ | $q_1$ | $0.0 \pm 0.02 \pm 0.04$ |
| $\Sigma_2$ | $1.0 \pm 0.04 \pm 0.07$ | $q_2$ | $0.0 \pm 0.04 \pm 0.07$ |
| $\Sigma_3$ | $1.2^{+1.0+2.1}_{-0.90-1.2}$ | $q_3$ | $-0.07 \pm 0.17^{+0.36}_{-0.31}$ |
| $\Sigma_4$ | $0.84^{+0.62+1.3}_{-0.60-0.83}$ | $q_4$ | $-0.06 \pm 0.43^{+0.90}_{-0.69}$ |
| $\mu_1$ | $0.93 \pm 0.17^{+0.38}_{-0.28}$ | $q_5$ | $-0.12 \pm 0.62^{+1.2}_{-1.0}$ |
| $\mu_2$ | $0.93 \pm 0.20^{+0.44}_{-0.34}$ | $q_6$ | $0.30^{+1.3+2.7}_{-1.3-1.9}$ |
| $\mu_3$ | $0.95^{+0.85+1.8}_{-0.71-0.91}$ | $q_7$ | $-0.17^{+1.5+3.4}_{-1.1-1.8}$ |
| $\mu_4$ | $0.89^{+0.76+1.7}_{-0.66-0.84}$ | $q_8$ | $-0.31^{+1.9+4.1}_{-1.7-4.0}$ |

## V. CONCLUSION AND DISCUSSION

We have tested GR with current cosmological data, using a framework in which the departures from GR are encoded as modifications of the anisotropy and Poisson equations; these equations specify, respectively, how the metric perturbations relate to each other, and how they are sourced by perturbations in the energy-momentum tensor of matter. The modifications were parametrized with two functions $\{\eta, \mu\}$ (or alternatively $\{\Sigma, \mu\}$) that reduce to unity in GR. We have then explored the constraints on these functions in two ways. First, we have allowed them to evolve from unity at high redshifts to a different value today in a scale-independent way. Second, we have *pixelized them in both scale and redshift* and performed a Principal Component Analysis (PCA), following the ideas of [26, 30] — a first general study of this kind. Specifically, we have used a $2\times2$ pixellation for each function, thus having 8 modified gravity parameters. In order to remove the covariance between the bins, and to analyze which modes are best constrained, we have then performed a 2D PCA of the results, obtaining constraints on the 8 derived de-correlated parameters.

We have used currently available data constraining both the background expansion history and the evolution of scalar perturbations in the Universe. In particular, we have used a combined measurement of the ISW effect through correlation of galaxies with CMB, the latest available supernovae Type Ia data including those from the SDSS, the CMB temperature and polarization spectra from WMAP5, and weak lensing data from the CFHTLS shear catalog. We have kept the analysis conservative by excluding small-scale data in the strongly non-linear regime, and we have checked and excluded possible tensions between the data sets by analyzing them individually before combining them.

Throughout the paper, we have assumed a flat ΛCDM background and tried to constrain deviations from GR in the evolution of matter and metric perturbations. In the simplest case, where the MG functions $\{\mu, \Sigma\}$ were allowed a single transition in redshift, we have found no evidence for a departure from GR, in agreement with other works. We find that the ISW effect, probed through the CMB auto-correlation and the cross-correlation with galaxy maps, currently gives the strongest constraint on $\Sigma$ because it is sensitive to the change of the lensing potential, $\Phi + \Psi$, at the transition.

In the pixellated case, we have found that one of the PCA eigenmodes shows a $2\sigma$ deviation from GR. However, this anomalous mode is due to the "bump" feature in the CFHTLS lensing data, which is most likely due to a systematic effect [34], combined with a preference for higher $\Omega_m$ by the SNe data. A separate analysis which

does not include WL data shows indeed good agreement with GR. A better understanding of systematic effects in both WL and SNe data sets needs to be achieved before any such discrepancy is viewed as a deviation from GR.

Even though this is most likely due to a known systematic effect, we emphasize that we would not have found this deviation if $\Sigma$ were taken to be scale-independent. In such case, the change in $\Sigma$ would be significantly constrained by the ISW effect. The PCA analysis using two bins in $k$ for $\Sigma$ could successfully isolate the strong constraint from the ISW effect and pick up a feature in WL. This demonstrates that the same data can lead to a higher level of detection of deviations from an expected model if more flexibility is allowed in the parametrization. Thus, when fitting $\mu(k,z)$ and $\eta(k,z)$ to data, it is important that their parametrization allows for some scale-dependence. Otherwise, one might risk missing a systematic effect or a real departure from GR, and thus would not be exploiting the true discovery potential of the data.

Finally, we comment on other recent studies that reported constraints on deviations from GR using current cosmological observations. In [33], the COSMOS weak lensing tomography data [9] were used together with SNe, CMB, BAO and the ISW-galaxy cross correlation. [32] found that the constraints from CMB+SNe+CFHTLS without COSMOS were indistinguishable from those including COSMOS and they did not find any deviations from GR. They argued that the sky coverage of CFHTLS is more important than the redshift depth of COSMOS. Also it should be noted that weak lensing measurements in COSMOS are made on strongly non-linear scales and there is an ambiguity in modeling the non-linear power spectrum.

In [32], a similar set of data to that described here was used to constrain two functions that are combinations of $\mu$ and $\eta$. The differences between our study and that of [32] include: (1) we used the ISW cross-correlation data; (2) we excluded small-scale modes in the CFHTLS data to avoid the strongly non-linear regime; (3) we simultaneously constrained two functions $\mu$ and $\eta$ while [32] varied only one of the parameters when they use 3 bins in $z$; (4) scale dependence was allowed in our paper; and (5) we used the Fisher matrix based PCA approach to make a decision on how many pixels to use. Their results are qualitatively consistent with the result of our first parametrization.

Further improvements of this technique will be possible with a new generation of LSS data (e.g. DES, Pan-STARRS, LSST, Euclid), which will dramatically increase the number of modes with sufficient signal-to-noise. Finally, peculiar velocity data will provide an additional valuable probe for our approach, since they can constrain $\mu$ directly [52], thus breaking the $\Sigma$-$\mu$ degeneracy.

### Acknowledgments

We are grateful to Liping Fu, Martin Kilbinger and Yannick Mellier for permission to use the CFHTLS data in this paper, and to Catherine Heymans, Ludovic Van Waerbeke and Ismael Tereno for valuable comments on an earlier version of the draft. We also thank Robert Crittenden for useful discussions. The computations were performed on the Western Canada Research Grid (WestGrid) facility. TG acknowledges support from the Alexander von Humboldt Foundation. LP is supported by an NSERC Discovery Grant. AS is supported by the grant NSF AST-0708501. GZ, DB, KK, RCN and YSS are supported by STFC. DB and KK are also supported by RCUK. KK acknowledges support from the European Research Council.

[1] D. Larson *et al.*, arXiv:1001.4635 [astro-ph.CO].
[2] E. Komatsu *et al.*, arXiv:1001.4538 [astro-ph.CO].
[3] W. J. Percival *et al.*, arXiv:0907.1660 [astro-ph.CO].
[4] R. Kessler *et al.*, Astrophys. J. Suppl. **185**, 32 (2009) [arXiv:0908.4274 [astro-ph.CO]].
[5] R. K. Sachs and A. M. Wolfe, Astrophys. J. **147** (1967) 73 [Gen. Rel. Grav. **39** (2007) 1929].
[6] R. G. Crittenden and N. Turok, Phys. Rev. Lett. **76** (1996) 575 [arXiv:astro-ph/9510072].
[7] T. Giannantonio *et al.*, Phys. Rev. D **77**, 123520 (2008)
[8] S. Ho, C. Hirata, N. Padmanabhan, U. Seljak and N. Bahcall, Phys. Rev. D **78** (2008) 043519 [arXiv:0801.0642 [astro-ph]].
[9] R. Massey *et al.*, Astrophys. J. Suppl. **172**, 239 (2007) [arXiv:astro-ph/0701480].
[10] T. Schrabback *et al.*, arXiv:0911.0053 [astro-ph.CO].
[11] L. Fu *et al.*, Astron. Astrophys. **479**, 9 (2008).
[12] M. Kilbinger *et al.*, Astron. Astrophys. **497**, 677 (2009).
[13] `http://www.darkenergysurvey.org/`
[14] `http://pan-starrs.ifa.hawaii.edu`
[15] `http://www.lsst.org`
[16] A. Cimatti *et al.*, arXiv:0912.0914 [astro-ph.CO].
[17] E. V. Linder and R. N. Cahn, Astropart. Phys. **28**, 481 (2007)
[18] R. Caldwell, A. Cooray and A. Melchiorri, Phys. Rev. D **76**, 023507 (2007)
[19] P. Zhang, M. Liguori, R. Bean and S. Dodelson, Phys. Rev. Lett. **99**, 141302 (2007) [arXiv:0704.1932 [astro-ph]].
[20] L. Amendola, M. Kunz and D. Sapone, JCAP **0804**, 013 (2008)
[21] W. Hu and I. Sawicki, Phys. Rev. D **76**, 104043 (2007)
[22] V. Acquaviva, A. Hajian, D. N. Spergel and S. Das, Phys. Rev. D **78**, 043514 (2008) [arXiv:0803.2236 [astro-ph]].
[23] J. P. Uzan, Gen. Rel. Grav. **39**, 307 (2007) [arXiv:astro-ph/0605313].
[24] E. Bertschinger and P. Zukin, Phys. Rev. D **78** (2008) 024015

[25] G. B. Zhao, L. Pogosian, A. Silvestri and J. Zylberberg, Phys. Rev. D **79**, 083513 (2009).

[26] L. Pogosian, A. Silvestri, K. Koyama and G. B. Zhao, arXiv:1002.2382 [astro-ph.CO].

[27] B. Jain and P. Zhang, Phys. Rev. D **78**, 063503 (2008) [arXiv:0709.2375 [astro-ph]].

[28] Y. S. Song and K. Koyama, JCAP **0901**, 048 (2009) [arXiv:0802.3897 [astro-ph]].

[29] Y. S. Song and O. Dore, JCAP **0903** (2009) 025 [arXiv:0812.0002 [astro-ph]].

[30] G. B. Zhao, L. Pogosian, A. Silvestri and J. Zylberberg, Phys. Rev. Lett. **103**, 241301 (2009)

[31] S. F. Daniel, R. R. Caldwell, A. Cooray and A. Melchiorri, Phys. Rev. D **77**, 103513 (2008) [arXiv:0802.1068 [astro-ph]].

[32] S. F. Daniel, E. V. Linder, T. L. Smith, R. R. Caldwell, A. Cooray, A. Leauthaud and L. Lombriser, arXiv:1002.1962 [astro-ph.CO].

[33] R. Bean and M. Tangmatitham, arXiv:1002.4197 [astro-ph.CO].

[34] CFHTLenS team private communication; we note that this is a known systematic issue, due to residual field-to-field variations in shear estimation on the scale of the camera field-of-view.

[35] `http://terapix.iap.fr/rubrique.php?id_rubrique=169`

[36] P. Schneider, L. van Waerbeke, B. Jain and G. Kruse, Mon. Not. Roy. Astron. Soc. **296**, 873 (1998).

[37] E. Beynon, D. J. Bacon and K. Koyama, arXiv:0910.1480 [astro-ph.CO].

[38] E. Komatsu *et al.* [WMAP Collaboration], Astrophys. J. Suppl. **180**, 330 (2009).

[39] J. Dunkley, *et al.*, arXiv: 0803.0586; E. L. Wright, *et al.*, arXiv: 0803.0577;
M. R. Nolta, *et al.*, arXiv: 0803.0593;
B. Gold, *et al.*, arXiv: 0803.0715;
G. Hinshaw, *et al.*, arXiv: 0803.0732.

[40] A. G. Riess *et al.*, Astrophys. J. **699**, 539 (2009).

[41] S. Burles, K. M. Nollett and M. S. Turner, Astrophys. J. **552**, L1 (2001).

[42] N. Afshordi, G. Geshnizjani and J. Khoury, JCAP **0908**, 030 (2009)

[43] D. Wands, K. A. Malik, D. H. Lyth and A. R. Liddle, Phys. Rev. D **62**, 043527 (2000)

[44] E. Bertschinger, Astrophys. J. **648**, 797 (2006)

[45] A. Lewis, A. Challinor and A. Lasenby, Astrophys. J. **538**, 473 (2000) [arXiv:astro-ph/9911177].

[46] T. Giannantonio, M. Martinelli, A. Silvestri and A. Melchiorri, arXiv:0909.2045 [astro-ph.CO].

[47] D. Huterer and G. Starkman, Phys. Rev. Lett. **90**, 031301 (2003)

[48] R. G. Crittenden, L. Pogosian and G. B. Zhao, JCAP **0912**, 025 (2009)

[49] G. B. Zhao and X. Zhang, Phys. Rev. D **81**, 043518 (2010) [arXiv:0908.1568 [astro-ph.CO]].

[50] A. J. S. Hamilton and M. Tegmark, Mon. Not. Roy. Astron. Soc. **312**, 285 (2000)

[51] A. Lewis and S. Bridle, Phys. Rev. D **66** 103511 (2002).

[52] Y. -S. Song, *et al.* in preparation.